Available online at www.sciencedirect.com
ScienceDirect
International Journal of Heat and Mass Transfer 50 (2007) 2492–2502
International Journal of HEAT and MASS TRANSFER
www.elsevier.com/locate/ijhmt

A novel solution for pressure drop in singly connected microchannels of arbitrary cross-section

Majid Bahrami [a,*], M. Michael Yovanovich [b], J. Richard Culham [b]

[a] Department of Mechanical Engineering, University of Victoria, Victoria, BC, Canada V8W 3P6
[b] MHTL, Department of Mechanical Engineering, University of Waterloo, Canada

Received 3 August 2006; received in revised form 1 December 2006

Abstract

This paper outlines a novel approximate solution for determining the pressure drop of fully developed, laminar, single-phase flow in singly connected microchannels of arbitrary cross-section. Using a "bottom-up" approach, it is shown that for constant fluid properties and flow rate in fixed cross-section channels, the Poiseuille number is only a function of geometrical parameters of the cross-section, i.e., perimeter, area, and polar moment of inertia. The proposed model is validated with experimental data for rectangular, trapezoidal, and triangular microchannels. The model is also compared against numerical results for a wide variety of channel cross-sections including: hyperellipse, trapezoid, sine, square duct with two adjacent round corners, rhombic, circular sector, circular segment, annular sector, rectangular with semi-circular ends, and moon-shaped channels. The model predicts the pressure drop for the cross-sections listed within 8% of the values published.

Keywords: Laminar fully developed flow; Microchannels; Pressure drop; Modeling; Saint-Venant; Poisson's equation; Characteristic length scale; Arbitrary cross-section channels

1. Introduction

Micro fabrication technologies make it possible to build micro-fluidic, silicon-based microchannels of different cross-sections in microsystems such as micro-heat sinks, micro-biochips, micro-reactors and micro-nozzles. Transport phenomena in microchannels have been the focus of a large number of studies, e.g. [1–5]. Microchannels are also being used as gas delivery systems and heat exchangers in fuel cell technologies. Microchannels offer high surface area per volume ratios, high heat transfer coefficients, and low thermal resistances [6]. Microchannels can be produced directly by techniques such as chemical etching on silicon wafers. As a result, the cross-section of the channels depends on a variety of factors, such as the crystallographic nature of the silicon used. When a KOH-anisotropic etching technique is employed, microchannels with fixed cross-sections are obtained [7]. The shape of the cross-section depends on the orientation of the silicon crystal planes. For instance, the microchannels etched in $\langle 1\,0\,0\rangle$ or in $\langle 1\,1\,0\rangle$ silicon will have a trapezoidal cross-section with an apex angle of 54.7° imposed by the crystallographic morphology of the silicon or a rectangular cross-section, respectively [7].

In recent years, a large number of experimental studies have focused on the pressure drop of laminar flow of liquids in microchannels with various cross-sections, see [8–11]. However, published results are often inconsistent. According to Pfund et al. [12], some of these authors conducted experiments in non-circular microchannels, but compared their pressure drop data with the classical values of $fRe = 16$ or 64 of circular pipes. Recently, Liu and

* Corresponding author.
E-mail addresses: mbahrami@uvic.ca (M. Bahrami), mmyov@mhtlab.uwaterloo.ca (M. Michael Yovanovich), rix@mhtlab.uwaterloo.ca (J. Richard Culham).

0017-9310/$ - see front matter © 2007 Elsevier Ltd. All rights reserved.
doi:10.1016/j.ijheatmasstransfer.2006.12.019

Nomenclature

A	cross-sectional area, m^2
a, b, c	dimensions of channel cross-section, m
D_h	hydraulic diameter $4A/P$, m
$E(\cdot)$	complete elliptic integral of second kind
f	Fanning friction factor, $2\bar{\tau}/\rho\bar{w}^2$
I_p	polar moment of inertia, m^4
I_p^*	specific polar moment of inertia, I_p/A^2
L	channel length, m
n	exponent, hyperellipse parameter
P	perimeter, m
Po	Poiseuille number
$Re_{\sqrt{A}}$	Reynolds number, $\rho\bar{w}\sqrt{A}/\mu$
w	fluid velocity, m/s
$\bar{w}$	mean fluid velocity, m/s

Greek symbols

α	aspect ratio trapezoidal duct, b/a
β	dimensionless parameter, Eq. (26)
γ	dimensionless parameter, Eq. (26)
ϵ	aspect ratio
ρ	fluid density, kg/m^3
μ	dynamic viscosity, kg/m s
τ	wall shear stress, N/m^2
ϕ	trapezoidal channel angle, rad
Δp	pressure drop, Pa
$\Gamma(\cdot)$	gamma function

Subscripts

$\sqrt{A}$	square root of cross-sectional area, m
L	lateral

Garimella [13] and Wu and Cheng [14] conducted experiments in *smooth* rectangular and trapezoidal microchannels, respectively. They reported that the Navier–Stokes equations are valid for laminar flow in smooth microchannels (micron size dimensions). Some of the discrepancies observed in the published data can be explained within the limits of continuum fluid mechanics and are due to wall roughness of microchannels. Bahrami et al. [15] developed an analytical model that predicts the observed trends in randomly *rough* microchannels to a certain degree.

Finding analytical solutions for many practical singly connected cross-sections, such as trapezoidal microchannels, is complex and/or impossible. In many engineering applications such as basic design and optimization, it is often required to obtain the trends and a reasonable estimate of the pressure drop. Muzychka and Yovanovich [16,17] introduced a geometrical mapping for predicting the pressure drop of fully developed, laminar flow in non-circular channels; in which non-circular ducts are mapped into equivalent rectangular channels. They proposed the use of the square root of cross-sectional area as the characteristics length instead of the hydraulic diameter. Comparing the rectangular mapping model with published numerical results, they have demonstrated that the $fRe_{\sqrt{A}}$, is a weak function of the geometry of the cross-section. This method [16], however, requires an equivalent rectangle which may not be applicable to the general case of "arbitrary cross-section".

The goal of this paper is to develop an accurate approximate model that can predict the pressure drop for singly connected channels of arbitrary cross-section. The proposed model is compared with experimental and/or numerical data for singly connected channels such as: *rectangular, elliptical, triangular, hyperellipse, trapezoid, sine, square duct with two adjacent round corners, rhombic, circular sector, circular segment, annular sector, rectangular with semi-circular ends*, and *moon-shaped*. After successful validation of the model with these channels, the analysis can be expanded to the general case of *arbitrary cross-section*. However; the use of present model is not recommended for doubly connected channels such as annular ducts since it fails to predict accurate results. The model estimates the pressure drop of the cross-sections listed above within approximately 8% accuracy and provides a powerful tool for basic designs, parametric studies, and optimization analyses required for applications such as in microchannel heat exchangers and heat sinks.

2. Proposed model

The assumptions of the present model can be summarized as:

- fully developed, steady-state, laminar, and continuum flow
- constant cross-sectional area A and constant perimeter P
- constant fluid properties
- negligible slip-on-the-wall and surface effects, body forces such as gravity, centrifugal, Coriolis, and electromagnetic.

For such a flow, the Navier–Stokes equations reduce to the momentum equation. This is Poisson's equation in one or two dimensions depending on the cross-sectional geometry [18]. In this case, the "source" term in Poisson's equation is the constant pressure drop along the length of the duct:

$$\nabla^2 w = \frac{1}{\mu}\frac{\mathrm{d}p}{\mathrm{d}z} \quad \text{with} \quad w = 0 \text{ on the boundary} \tag{1}$$

where $w = w(x, y)$ and z are the fluid velocity and the flow direction, respectively. The boundary condition for the velocity is the no-slip condition on the wall. The velocity profile is constant in the longitudinal direction; thus the pressure gradient applied at the ends of the channel must be balanced by the shear stress on the wall of the channel

$$\bar{\tau} PL = \Delta p A \tag{2}$$

where

$$\bar{\tau} = \frac{1}{A_\mathrm{L}} \int \int_{A_\mathrm{L}} \tau \, \mathrm{d}A_\mathrm{L}$$

where A_L is the lateral surface area, L is the channel length, and $\bar{\tau}$ is the mean wall shear stress.

The proposed model is based on the analytical solution of the elliptical channel, not because it is likely to occur in practice, but rather to utilize the unique geometrical property of its velocity solution.

In this section, first we show through analysis that the square root of the cross-sectional area is a "more appropriate" choice for the characteristic length scale of arbitrary cross-section channels.

Using the analytical solution [19,20], the *mean velocity* $\bar{w}$ for the laminar fluid flow in elliptical ducts is:

$$\bar{w} = \frac{b^2 c^2}{4(b^2 + c^2)} \frac{\Delta p}{\mu L} \tag{3}$$

where b and c are the major and minor semi-axes of the cross-section, $b \geqslant c$. An aspect ratio can be defined for the elliptical microchannel

$$0 < \epsilon \equiv \frac{c}{b} \leqslant 1 \tag{4}$$

For an elliptical channel, the cross-sectional area and the perimeter are:

$$\left.\begin{aligned} A &= \pi bc \\ P &= 4bE(\sqrt{1-\epsilon^2}) \end{aligned}\right\} \tag{5}$$

where $E(x) = \int_0^{\pi/2} \sqrt{1 - x^2 \sin^2 t}\, \mathrm{d}t$ is the complete elliptic integral of the second kind. The mean velocity, Eq. (3), can be written in terms of the aspect ratio, ϵ,

$$\bar{w} = \frac{c^2}{4(1+\epsilon^2)} \frac{\Delta p}{\mu L} \tag{6}$$

Combining Eqs. (2), (5), and (6), the mean wall shear stress becomes:

$$\bar{\tau} = \frac{4(1+\epsilon^2)\bar{w}}{c^2} \frac{\mu A}{P} \tag{7}$$

Substituting for the area and perimeter of the elliptical duct, the mean wall shear stress becomes:

$$\bar{\tau} = \frac{\pi(1+\epsilon^2)}{E(\sqrt{1-\epsilon^2})} \frac{\mu \bar{w}}{c} \tag{8}$$

A relationship can be found between the minor axis c and the aspect ratio from the cross-sectional area, $c = \sqrt{A\epsilon/\pi}$. Substituting c into Eq. (8), one finds:

$$\bar{\tau} = \frac{\pi\sqrt{\pi}(1+\epsilon^2)}{\sqrt{\epsilon} E\left(\sqrt{1-\epsilon^2}\right)} \frac{\mu \bar{w}}{\sqrt{A}} \tag{9}$$

It is conventional to use the ratio of area over perimeter $D_\mathrm{h} = 4A/P$, known as the *hydraulic diameter*, as the characteristic length scale for non-circular channels. Using D_h is an arbitrary choice; however, as can be seen in Eq. (9), the *square root of area,* $\sqrt{A}$, is a more appropriate length scale since it is found through analysis.

With the square root of area, $\sqrt{A}$, as the characteristic length scale, a non-dimensional wall shear stress can be defined as:

$$\bar{\tau}^* \equiv \frac{\bar{\tau}\sqrt{A}}{\mu \bar{w}} = \frac{\pi\sqrt{\pi}(1+\epsilon^2)}{\sqrt{\epsilon} E(\sqrt{1-\epsilon^2})} \tag{10}$$

It should be noted that the right hand side of Eq. (10) is only a function of the aspect ratio (geometry) of the channel.

Using Eq. (9), the Fanning friction factor, defined as $f \equiv 2\bar{\tau}/\rho \bar{w}^2$ for elliptical microchannels becomes:

$$f = \frac{2\pi\sqrt{\pi}(1+\epsilon^2)}{\sqrt{\epsilon} E\left(\sqrt{1-\epsilon^2}\right)} \frac{\mu}{\rho \bar{w} \sqrt{A}} \tag{11}$$

The Reynolds number can be defined based on the square root of area, $\sqrt{A}$

$$Re_{\sqrt{A}} = \frac{\rho \bar{w} \sqrt{A}}{\mu} \tag{12}$$

Eq. (11) can be re-written

$$fRe_{\sqrt{A}} = \frac{2\pi\sqrt{\pi}(1+\epsilon^2)}{\sqrt{\epsilon} E\left(\sqrt{1-\epsilon^2}\right)} \tag{13}$$

Similar to $\bar{\tau}^*$, $fRe_{\sqrt{A}}$ is only a function of the geometry of the channel. Thus, a relationship can be found between the non-dimensional friction factor $\bar{\tau}^*$ and $fRe_{\sqrt{A}}$

$$fRe_{\sqrt{A}} = 2\bar{\tau}^* \tag{14}$$

The method described above, for elliptical channels, can be applied for other shapes that have analytical solutions such as rectangular channels, see [19,20] for details of analytical solutions. Following the same steps, the friction factor Reynolds number product based on the square root of the cross-sectional area for rectangular ducts is:

$$fRe_{\sqrt{A}} = \frac{12}{\left[1 - \frac{192}{\pi^5}\epsilon \tanh\left(\frac{\pi}{2\epsilon}\right)\right](1+\epsilon)\sqrt{\epsilon}} \tag{15}$$

The original analytical solution for the mean velocity in rectangular channels is in the form of a series. However, when $\epsilon = 1$ (square), the first term of the series gives the value $fRe_{\sqrt{A}} = 14.132$ compared with the exact value (full series solution) of 14.23. The maximum difference of

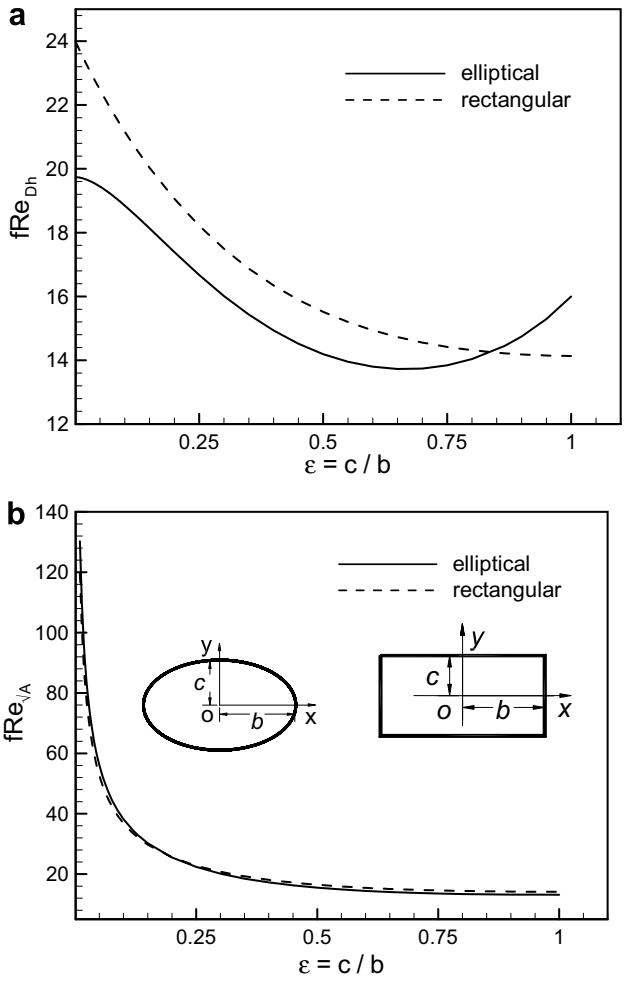

Fig. 1. Comparison between analytical solutions of fRe for elliptical and rectangular ducts using: (a) hydraulic diameter and (b) square root of area as characteristic length.

approximately 0.7% occurs at $\epsilon = 1$. For smaller values of ϵ, the agreement with the full series solution is even better [20]. Therefore, only the first term is employed in this study.

Fig. 1a and b show the comparison of the *analytical* solutions of fRe, for elliptical and rectangular cross-sections based on the hydraulic diameter and the square root of area, respectively. From Fig. 1 one clearly observes that using the square root of area as the characteristic length leads to similar trends in analytical solutions of fRe for elliptical and rectangular ducts. With respect to analytical solutions of $fRe_{\sqrt{A}}$ for rectangular and elliptical ducts, i.e., Eqs. (13) and (15) the following should be noted:

(1) for rectangular microchannels, two asymptotes can be recognized, i.e., the very narrow rectangular and square channels [17]

$$fRe_{\sqrt{A}} = \begin{cases} 12/\sqrt{\epsilon} & \epsilon \to 0 \\ 14.132 & \epsilon = 1 \end{cases} \tag{16}$$

(2) for elliptical microchannels, the asymptotes are the very narrow elliptical and circular microchannels [17]

$$fRe_{\sqrt{A}} = \begin{cases} 11.15/\sqrt{\epsilon} & \epsilon \to 0 \\ 14.179 & \epsilon = 1 \end{cases} \tag{17}$$

Note that the $fRe_{\sqrt{A}}$ values and trends for elliptical and rectangular channels are very close at both asymptotes, see Fig. 1b. In spite of the different forms of the $fRe_{\sqrt{A}}$ for rectangular and elliptical microchannels, trends of both formulae are very similar as the aspect ratio varies between $0 < \epsilon \leqslant 1$. The maximum relative difference is less than 8%. which occurs for small values of ϵ.

Elliptical and rectangular cross-sections cover a wide range of singly connected microchannels. With the similarity in the trends of the solutions for these cross-sections, one can conclude that a general, *purely geometrical*, relationship exists that predicts $fRe_{\sqrt{A}}$ for arbitrary singly connected cross-sections. Based on this observation, an *approximate model* is developed in this section.

2.1. Saint-Venant principle

Torsion in beams and fully developed, laminar flow in ducts are similar in the sense that the governing equation for both problems is Poisson's equation, Eq. (1). Comparing various singly connected cross-sections, Saint-Venant 1880 found that the torsional rigidity can be approximated by replacing the given shaft by the shaft of an elliptic cross-section having the same cross-sectional area and the same polar moment of inertia as the given shaft [21]. Using Saint-Venant's concept, the present model employs the analytical solution of the elliptical duct to approximate the pressure drop in channels of arbitrary cross-section.

The polar moment of inertia, $I_p = \int_A (x^2 + y^2) dA$, for an ellipse is

$$I_p = \frac{\pi bc(b^2 + c^2)}{4} \tag{18}$$

Eq. (6) can be re-arranged in terms of the polar moment of inertia, about its center, as follows:

$$\frac{\Delta p}{L} = \frac{16\pi^2 \mu \bar{w}}{A^3} I_p = \frac{16\pi^2 \mu \bar{w}}{A} I_p^* \tag{19}$$

where $I_p^* = I_p/A^2$ is a non-dimensional geometrical parameter which we call the *specific polar moment of inertia*. Combining Eqs. (2) and (19), one can write

$$\bar{\tau} = \frac{16\pi^2 \mu \bar{w}}{\sqrt{A}} \frac{\sqrt{A}}{P} I_p^* \tag{20}$$

Note that $\sqrt{A}/P$ is also a non-dimensional geometrical parameter. Using Eq. (20), the Fanning friction factor can be determined

$$fRe_{\sqrt{A}} = 32\pi^2 I_p^* \frac{\sqrt{A}}{P} \tag{21}$$

The right hand side of Eq. (21) only contains general geometrical characteristics of the cross-section, i.e., I_p, A, and

P. Therefore, the proposed model postulates that for constant fluid properties and flow rate, $fRe_{\sqrt{A}}$ is only a function of the non-dimensional geometrical parameter, $I_p^*\sqrt{A}/P$, of the cross-section.

Using the present model, a relationship can be derived for calculating the pressure drop of laminar, fully developed single-phase flow in arbitrary microchannels where $L \gg \sqrt{A}$:

$$\Delta p = 16\pi^2 \mu \bar{w} I_p^* \frac{L}{A} \tag{22}$$

To apply the present model, one should:

- find the center of geometry of the cross-section
- calculate geometrical parameters of the channel, i.e., perimeter P, cross-sectional area A, and polar moment of inertia I_p about the center of geometry, and determine $fRe_{\sqrt{A}}$ using Eq. (21).

Normally to find the friction factor: first Poisson's equation must be solved (numerically for most cross-sections) to find the velocity field, then the mean velocity and the mean wall shear stress should be calculated, and finally $fRe_{\sqrt{A}}$ should be determined. Applying the present model, on the other hand, one only needs to compute the non-dimensional parameter $I_p^*\sqrt{A}/P$ of the channel to determine $fRe_{\sqrt{A}}$. It clearly shows the convenience of the proposed model.

For more complex cross-sections such as moon-shaped ducts, the geometry often consists of simpler parts where the moment of inertia is known or easily calculated. The moment of inertia of the complex geometries about an axis can be found by *algebraic sum* of the moments of inertia of "simpler" geometries [22].

3. Comparison with experimental data

In this section, the present model is compared against experimental data collected by several researchers [13,14,23] for microchannels. The reported accuracy of the experimental data is on the order of 10%.

Wu and Cheng [14] conducted experiments and measured the friction factor of laminar flow of deionized water in a number of smooth silicon microchannels of trapezoidal cross-section over a range of Reynolds numbers.

The frictional resistance $fRe_{\sqrt{A}}$ is not a function of Reynolds number, i.e., it remains constant for the laminar regime as the Reynolds number varies. Therefore, the experimental data for each set are averaged over the laminar region. As a result, for each experimental data set, one value of $fRe_{\sqrt{A}}$ can be obtained. Table 1 summarizes geometric parameters of Wu and Cheng [14] microchannels; it also presents the predicted $fRe_{\sqrt{A}}$ values by the approximate model and the averaged values of the reported experimental values of $fRe_{\sqrt{A}}$. As shown in Table 1, the

Table 1
Trapezoidal microchannels data [14]

Channel	b (μm)	a (μm)	h (μm)	γ (–)	β (–)	$fRe_{\sqrt{A}}$		
						Model	Data	% Diffference
N1-100	100	20.1	56.4	1.06	0.56	13.85	14.48	−4.5
N1-150	150	70.1	56.4	1.95	0.87	15.61	15.95	−2.2
N1-200	200	120.2	56.4	2.84	0.94	18.34	18.74	−2.2
N1-500	500	420	56.5	8.14	0.99	33.38	31.55	5.5
N1-1000	1000	920	56.5	16.99	1.00	50.86	45.76	10.0
N1-4000	4000	3920	56.5	70.10	1.00	108.32	93.13	14.0
N2-50	50	0	35.3	0.71	0.00	13.50	13.95	−3.3
N2-100	100	39.9	42.4	1.65	0.82	14.83	14.91	−0.6
N2-150	150	89.9	42.4	2.83	0.94	18.29	18.22	0.4
N2-200	200	140	42.4	4.01	0.97	22.06	22.30	−1.1
N2-500	500	440	42.4	11.09	1.00	39.95	38.08	4.7
N2-1000	1000	940	42.4	22.89	1.00	59.94	54.60	8.9
N2-4000	4000	3940	42.4	93.70	1.00	125.76	110.70	12.0
N3-50	50	0	35.3	0.71	0.00	13.50	13.62	−0.9
N3-100	100	0	70.6	0.71	0.00	13.50	14.29	−5.8
N3-150	150	0	105.9	0.71	0.00	13.50	14.03	−3.9
N3-200	200	0	141.2	0.71	0.00	13.50	14.66	−8.6
N3-500	500	284	152.5	2.57	0.92	17.48	17.47	0.0
N3-1000	1000	784	152.5	5.85	0.99	27.46	26.45	3.7
N3-2000	2000	1784	152.5	12.40	1.00	42.59	39.57	7.1
N3-4000	4000	3784	152.5	25.52	1.00	63.57	57.07	10.2
N4-100	100	0	70.6	0.71	0.00	13.50	13.98	−3.5
N4-200	200	27.2	122.0	0.93	0.42	13.76	15.10	−9.7
N4-500	500	327	122.2	3.38	0.96	20.08	20.99	−4.5
N4-1000	1000	827	122.2	7.48	0.99	31.75	31.54	0.6
N4-4000	4000	3828	121.5	32.22	1.00	72.07	69.88	3.0
N5-150	150	47.4	72.5	1.36	0.73	14.24	14.87	−4.5
N6-500	500	279	156.1	2.50	0.92	17.24	17.07	1.0

microchannels tested by Wu and Cheng [14] cover a wide range of geometrical parameters, i.e., $0.71 \leqslant \gamma \leqslant 97.70$ and $0 \leqslant \beta \leqslant 1$ see Eq. (27), as a result the data include trapezoidal, triangular, and rectangular microchannels. It should be noted that, in spite of the different dimensions, channels N2-50, N3-50, N3-100, N3-150, N3-200, and N4-100 have the same values of β and γ; thus they are geometrically equivalent. It is interesting to observe that the predicted and the measured $fRe_{\sqrt{A}}$ values are identical for these channels, as expected. Fig. 2a shows the comparison between all data of Wu and Cheng [14] and the proposed model. The ±10% bounds of the model are also shown in the plot, to better demonstrate the agreement between the data and the model.

Liu and Garimella [13] carried out experiments and measured the friction factor in rectangular microchannels. They did not observe any scale-related phenomena in their experiments and concluded that the conventional theory can be used to predict the flow behavior in microchannels in the range of dimensions considered. They [13] measured and reported the relative surface roughness of the channels to be negligible, thus their channels can be considered smooth. Gao et al. [23] experimentally investigated laminar fully developed flow in rectangular microchannels. They designed their experiments to be able to change the height of the channels tested while the width remained constant at 25 mm. They conducted experiments with several channel heights. Gao et al. [23] measured the roughness of the channel and reported negligible relative roughness, thus their channels can be considered smooth.

Following the same method described for trapezoidal data, the reported values of $fRe_{\sqrt{A}}$ for rectangular microchannels [13,23] are averaged (over laminar region) and plotted against the model in Fig. 2b. As shown in Fig. 2b, the collected data cover a wide range of the aspect ratio $\epsilon = c/b$ (almost three decades). The relative difference between the data and the model is within the uncertainty of the experiments.

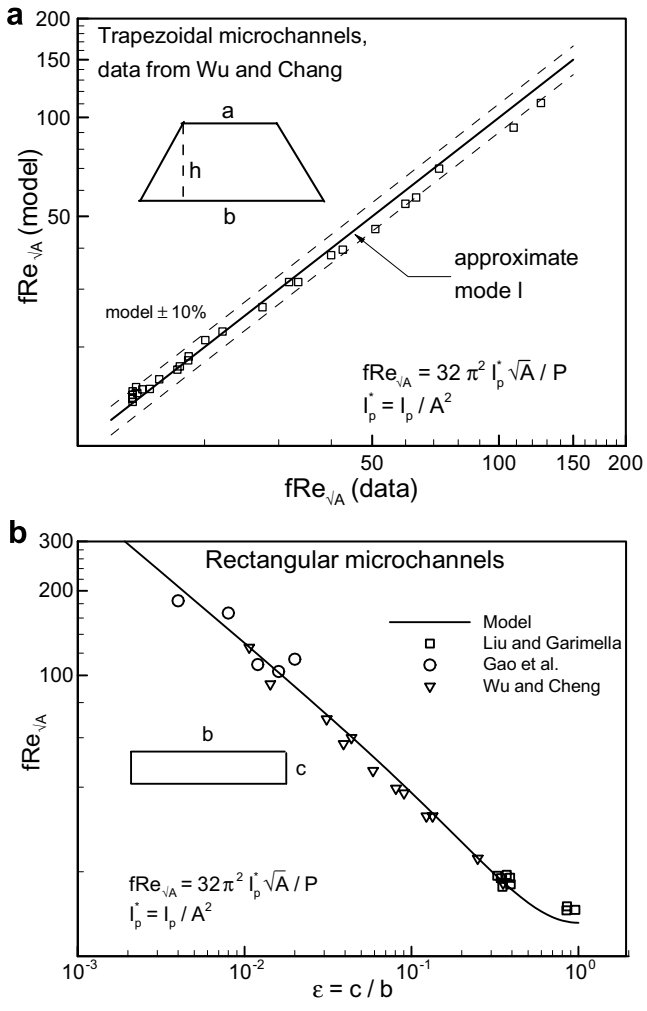

Fig. 2. Comparison of present model and experimental data for trapezoidal [14] and rectangular [13,14,23] microchannels.

4. Comparison with numerical results

In this section, the present model is compared with numerical results [18,24] for available cross-sections. Geometrical parameters needed to apply the model are reported for the cross-sections considered. The following relationship is used to convert the Reynolds number Fanning friction factor product based on D_h to $\sqrt{A}$

$$fRe_{\sqrt{A}} = \frac{P}{4\sqrt{A}} fRe_{D_h} \tag{23}$$

where $D_h = 4A/P$ is the hydraulic diameter of the channel.

4.1. Hyperellipse channel

A hyperellipse, in the first quadrant, is described by $y = b[1-(x/a)^n]^{1/n}$, where a and b are characteristic dimensions along the x and y axes, respectively, see Fig. 3. The effect of the parameter n on the shape of the hyperellipse channel is also shown in Fig. 3. When $n = 1$, the hyperellipse yields a rhombic duct $(a > b)$, and a square for $(a = b)$; at $n = 2$, the channel is elliptical $(a > b)$, and circular $(a = b)$; $n > 3$, it is rectangular $(a > b)$ or a square $(a = b)$ channel with rounded corners; and when $n \to \infty$, it approaches a full rectangle/square duct [25]. The cross-sectional area of a hyperellipse can be calculated from:

$$A = 4a^2\epsilon \frac{\sqrt{\pi}\Gamma\left(\frac{n+1}{n}\right)}{4^{1/n}\Gamma\left(\frac{n+2}{2n}\right)} \tag{24}$$

where $\Gamma(\cdot)$ is the gamma function and $\epsilon = b/a$ is the aspect ratio. The perimeter of the hyperellipse does not have a closed form solution and must be calculated numerically from, $P = 4\int_0^a \sqrt{1+(\mathrm{d}y/\mathrm{d}x)^2}\mathrm{d}x$. The polar moment of inertia of a hyperellipse about its center of geometry (origin) is:

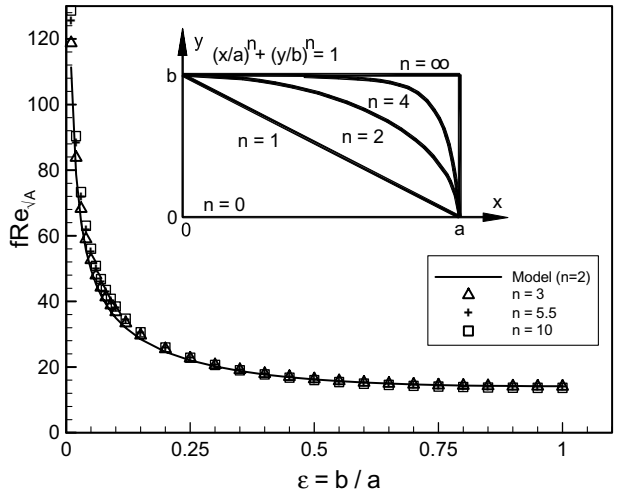

Fig. 3. Geometry and *fRe* predicted by model for hyperellipse channels for $n = 3,\ 5.5,\ 10$.

$$I_p = 4a^4\left[\frac{3\epsilon^3\Gamma\left(\frac{n+1}{n}\right)\Gamma\left(\frac{3}{n}\right) + \epsilon\Gamma\left(\frac{n+3}{n}\right)\Gamma\left(\frac{1}{n}\right)}{3n\Gamma\left(\frac{n+4}{n}\right)}\right] \tag{25}$$

It should be noted that the model is based on the analytical solution for elliptical channel which is a hyperellipse with $n = 2$. Also, the maximum difference between the elliptical $(n = 2)$ and rectangular $(n \to \infty)$ ducts analytical solutions is less than 8%. As a result, it can be concluded that the difference between the $fRe_{\sqrt{A}}$ predicted by the present model and that of a hyperellipse with any other value of $2 \leqslant n \leqslant \infty$ is less than 8%, as shown in Fig. 3. Fig. 3 also represents the $fRe_{\sqrt{A}}$ values predicted by the model for several values of $n = 3, 5.5,$ and 10 over aspect ratios $0.01 \leqslant \epsilon = b/a \leqslant 1$.

4.2. Trapezoidal channel

Trapezoidal cross-section is an important geometry since some microchannels are manufactured with trapezoidal cross-sections as a result of the etching process in silicon wafers. Furthermore, in the limit when the top side length goes to zero, it yields an isosceles triangle. At the other limit when top and bottom sides are equal, it becomes a rectangle/square. The cross-sectional area, perimeter, and polar moment of inertia (about its center) are: $A = 4b^2\gamma$, $P = 4b(\gamma + \sqrt{\gamma^2 - \beta\gamma^2 + 1})$, and

$$I_p = \frac{A^2[2(3\gamma^2+1) + \beta(1-3\gamma^2)]}{36\gamma}$$
$$\gamma \equiv \frac{1}{\alpha} + \frac{1}{\tan\phi} \quad \text{and} \quad \beta \equiv 1 - \frac{1}{\gamma^2\tan^2\phi} \tag{26}$$

where $\alpha = b/a$, defined in Shah and London [18]. Using Eq. (21), one can find $fRe_{\sqrt{A}}$:

$$fRe_{\sqrt{A}} = \frac{8\pi^2(3\gamma^2+1) + \beta(1-3\gamma^2)}{9\sqrt{\gamma}(\gamma + \sqrt{\gamma^2 - \beta\gamma^2 + 1})} \tag{27}$$

Shah and London [18] reported numerical values for fRe_{D_h} for laminar fully developed flow in a trapezoidal channel.

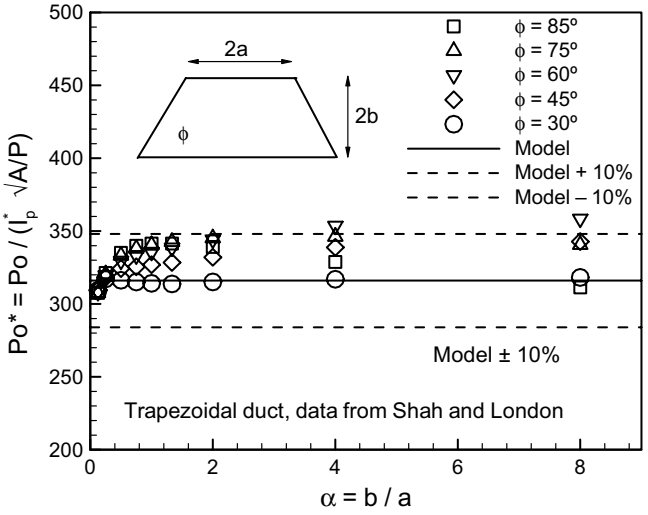

Fig. 4. Comparison between non-dimensional $fRe_{\sqrt{A}}$ predicted by the model and numerical results of Shah and London [18] for trapezoidal channel.

They presented fRe_{D_h} values as a function of $\alpha = b/a$ for different values of angles ϕ.

Fig. 4 shows the comparison between Eq. (27) and the numerical data reported by Shah and London [18]. For convenience, the comparison is presented using a non-dimensional form of $fRe_{\sqrt{A}}$

$$Po^* = \frac{fRe_{\sqrt{A}}}{I_p^*\sqrt{A}/P} \tag{28}$$

Note that based on the model, $Po^* = 32\pi^2 = 315.83$, see Fig. 4. Table 2 also shows the comparison between the approximate model and the numerical data reported by Shah and London [18]. As can be seen, except for a few points, the agreement between the approximate model and the numerical values is less than 8%.

4.3. Rhombic channel

Cross-sectional area, perimeter, and specific polar moment of inertia of a rhombic duct can be determined from; $A = L^2\sin\phi$, $P = 4L$, and $I_p^* = 1/(6\sin\phi)$, where L is the side of the rhombic duct. Using Eq. (21), $fRe_{\sqrt{A}}$ for the rhombic duct becomes

$$fRe_{\sqrt{A}} = \frac{4\pi^2}{3\sqrt{\sin\phi}} \tag{29}$$

Fig. 5a shows the comparison between numerical results [18] and Eq. (29). The maximum difference between the present model and numerical results is on the order of 8%.

4.4. Sine channel

The sine channel is represented by $y = b(1 + \cos\pi x/a)$. The center of geometry, area, and perimeter of a sine duct

Table 2
Model vs data [18], trapezoidal channels

α^*	fRe_{D_h}	γ	β	$fRe_{\sqrt{A}}$		
				Model	[18]	%Diffference
$\phi = 85°$						
8	17.474	0.212	0.830	23.384	23.054	1.41
4	16.740	0.337	0.933	18.563	19.325	−4.11
2	15.015	0.587	0.978	14.516	15.587	−7.38
4/3	14.312	0.837	0.989	13.318	14.398	−8.11
1	14.235	1.087	0.994	13.203	14.274	−8.11
3/4	14.576	1.421	0.996	13.774	14.825	−7.63
1/2	15.676	2.087	0.998	15.806	16.770	−6.10
1/4	18.297	4.087	1.000	22.648	23.038	−1.72
1/8	20.599	8.087	1.000	33.804	32.926	2.60
$\phi = 75°$						
8	14.907	0.393	0.535	15.745	16.982	−7.85
4	14.959	0.518	0.732	14.725	16.142	−9.62
2	14.340	0.768	0.878	13.499	14.754	−9.30
4/3	14.118	1.018	0.931	13.244	14.365	−8.46
1	14.252	1.268	0.955	13.520	14.576	−7.81
3/4	14.697	1.601	0.972	14.304	15.311	−7.04
1/2	15.804	2.268	0.986	16.430	17.332	−5.49
1/4	18.313	4.268	0.996	23.165	23.505	−1.47
1/8	20.556	8.268	0.999	34.155	33.254	2.64
$\phi = 60°$						
8	13.867	0.702	0.324	13.540	15.364	−13.47
4	13.916	0.827	0.513	13.544	15.162	−11.95
2	13.804	1.077	0.713	13.623	14.842	−8.95
4/3	13.888	1.327	0.811	13.953	14.960	−7.21
1	14.151	1.577	0.866	14.484	15.392	−6.26
3/4	14.637	1.911	0.909	15.384	16.230	−5.49
1/2	15.693	2.577	0.950	17.482	18.241	−4.34
1/4	18.053	4.577	0.984	23.908	24.184	−1.15
1/8	20.304	8.577	0.995	34.582	33.735	2.45
$\phi = 45°$						
8	13.301	1.125	0.210	14.669	15.921	−8.53
4	13.323	1.250	0.360	14.796	15.874	−7.28
2	13.364	1.500	0.556	15.123	15.899	−5.13
4/3	13.541	1.750	0.673	15.573	16.194	−3.99
1	13.827	2.000	0.750	16.125	16.691	−3.51
3/4	14.260	2.333	0.816	16.973	17.492	−3.06
1/2	15.206	3.000	0.889	18.869	19.377	−2.69
1/4	17.397	5.000	0.960	24.760	24.952	−0.77
1/8	19.743	9.000	0.988	34.958	34.268	1.97
$\phi = 30°$						
8	12.760	1.857	0.130	17.923	18.058	−0.75
4	12.782	1.982	0.236	18.013	18.077	−0.35
2	12.875	2.232	0.398	18.277	18.235	0.23
4/3	13.012	2.482	0.513	18.633	18.509	0.66
1	13.246	2.732	0.598	19.062	18.961	0.53
3/4	13.599	3.065	0.681	19.720	19.672	0.25
1/2	14.323	3.732	0.785	21.220	21.249	−0.14
1/4	16.284	5.732	0.909	26.178	26.295	−0.44
1/8	18.479	9.732	0.968	35.489	34.747	2.09

can be found from; $y_c = 3b/4$, $A = 2ab$, and $P = 2a + 4aE(\pi\sqrt{-\epsilon^2})$, respectively. The $fRe_{\sqrt{A}}$ becomes:

$$fRe_{\sqrt{A}} = 4\sqrt{2}\pi^2\left[\frac{\pi^2-6}{6\pi^2\epsilon}+\frac{13\epsilon}{96}\right]\frac{\sqrt{\epsilon}}{1+2E\left(\pi\sqrt{-\epsilon^2}\right)/\pi} \tag{30}$$

where $E(\cdot)$ is the complete elliptic integral of the second kind and $\epsilon = b/a$. Fig. 5b shows the comparison between numerical results from [18] and Eq. (30). The model presents the trends of the numerical results with a difference of 9.3%.

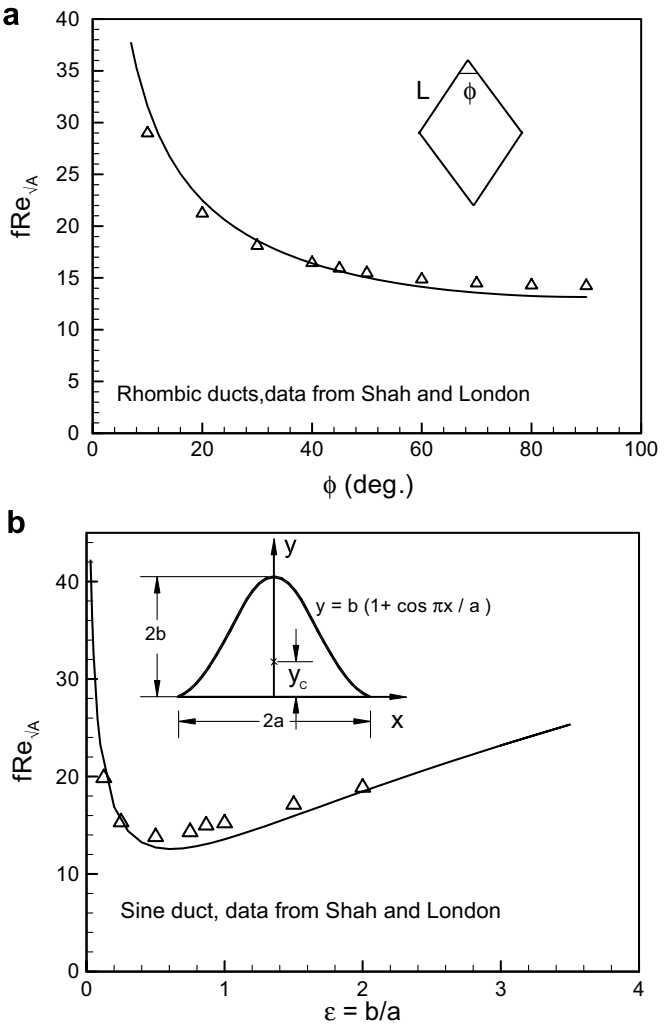

Fig. 5. Comparison of present model and numerical values [18] for rhombic and sine channels.

4.5. Circular sector channel

The center of geometry, area, polar moment of inertia, and perimeter of a circular sector duct can be found from; $x_c = 2a\sin\phi/3\phi$, $A = a^2\phi$, $I_p = a^4(9\phi^2 - 8\sin^2\phi)/18\phi$, and $P = 2a(1+\phi)$, respectively. The $fRe_{\sqrt{A}}$ becomes:

$$fRe_{\sqrt{A}} = \frac{8\pi^2\sqrt{\phi}(9\phi^2 - 8\sin^2\phi)}{9\phi^3(1+\phi)} \tag{31}$$

Fig. 6a shows the comparison between numerical results from Shah and London [18] and Eq. (31). The model presents the trends of the numerical results with a mean difference of 7.6%.

4.6. Circular segment channel

The cross-sectional area and perimeter of a circular segment duct can be found from; $A = a^2(\phi - 0.5\sin 2\phi)$

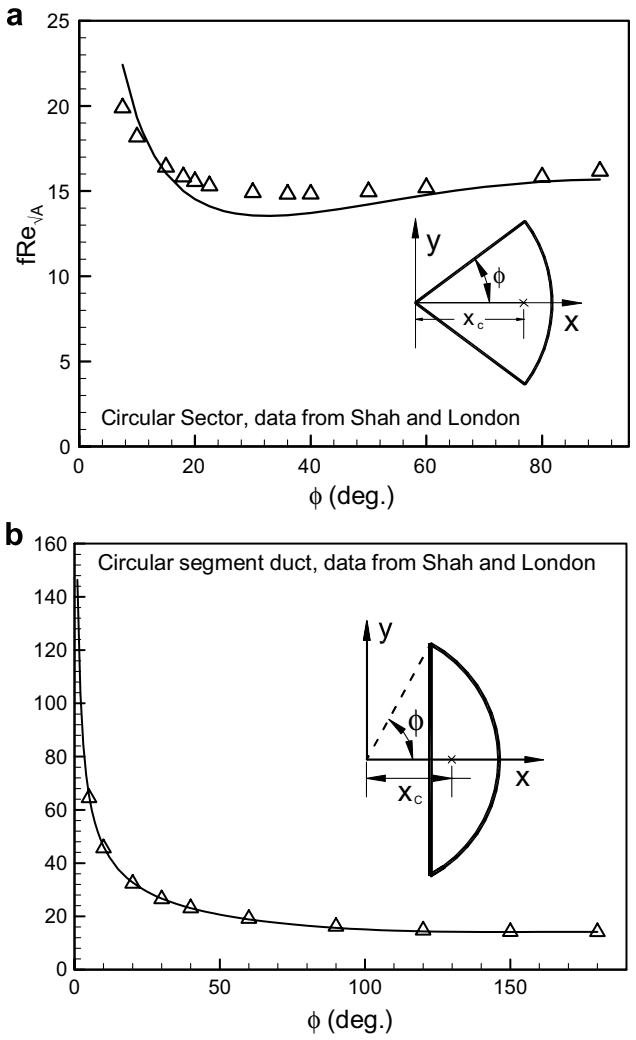

Fig. 6. Comparison of model and numerical values [18] for circular sector and circular segment channels.

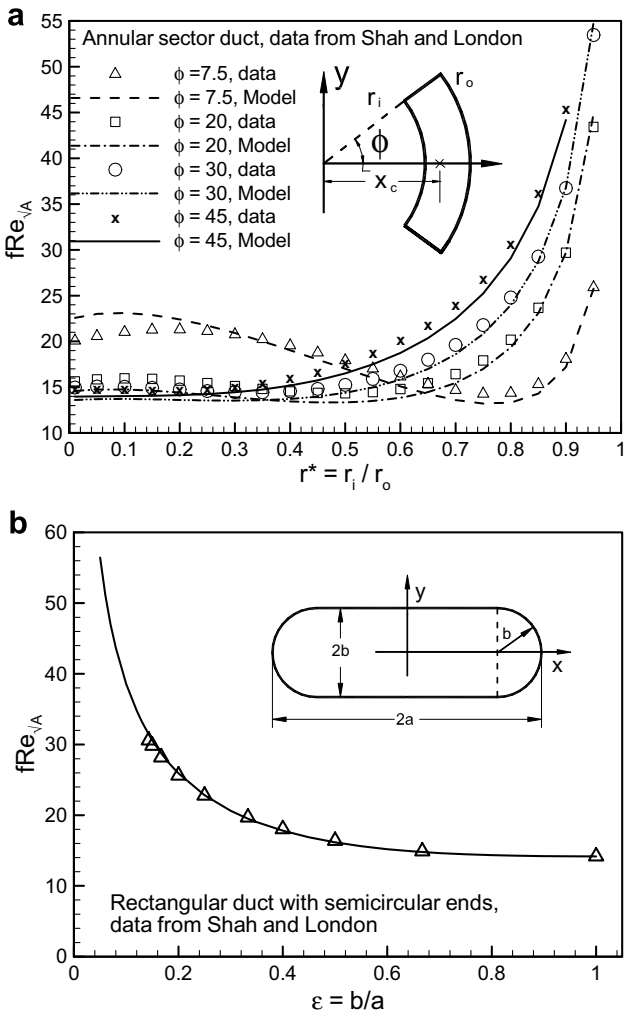

Fig. 7. Comparison of model and numerical values [18] for annular sector and rectangular duct with semi-circular ends.

and $P = 2a(\phi + \sin\phi)$. The polar moment of inertia about the center of geometry is:

$$I_p = a^4\left[\frac{\phi}{2} - \frac{\sin 2\phi(1+2\cos^2\phi)}{12} - \frac{(2\sin\phi - \cos\phi\sin 2\phi)^2}{9(\phi - 0.5\sin 2\phi)}\right]$$

Fig. 6b represents the comparison between the numerical results in Shah and London [18] and the present model. As seen, the present model shows excellent agreement with the numerical result with a maximum relative difference of 3.1%.

4.7. Annular sector channel

The center of geometry, area, polar moment of inertia, and perimeter of a circular sector duct can be found from; $A = \phi r_0^2(1-r^{*2})$ and $P = 2r_0[(1+r^*)\phi + 1 - r^*]$

$$x_c = \frac{2r_0\sin\phi}{3\phi}\frac{1-r^{*3}}{1-r^{*2}}$$

$$I_p^* = \frac{\frac{1}{2}(1-r^{*4}) - \frac{4}{9}\left(\frac{\sin\phi}{\phi}\right)^2\frac{(1-r^{*3})^2}{1-r^{*2}}}{\phi(1-r^{*2})^2}$$

where $r^* = r_i/r_0$. The $fRe_{\sqrt{A}}$ becomes:

$$fRe_{\sqrt{A}} = \frac{16\pi^2\sqrt{\phi(1-r^{*2})}\left[\frac{1}{2}(1-r^{*4}) - \frac{4}{9}\left(\frac{\sin\phi}{\phi}\right)^2\frac{(1-r^{*3})^2}{1-r^{*2}}\right]}{\phi(1-r^{*2})^2[(1+r^*)\phi + 1 - r^*]} \quad (32)$$

Fig. 7a represents the comparison between the numerical results in Shah and London [18] and the present model, Eq. (32). The present model shows good agreement with the numerical results for $2^\circ \leqslant \phi \leqslant 75^\circ$, with a maximum relative difference of less than 8%. However, the model fails for $\phi > 90^\circ$.

4.8. Rectangular channel with semi-circular ends

The cross-sectional area, perimeter, and polar moment of inertia of a circular sector duct can be found from; $A = a^2[4\epsilon(1-\epsilon) + \pi\epsilon^2/2]$ and $P = 2a(2 - 2\epsilon + \pi\epsilon)$ and

$$I_p = a^4\left[\frac{4\epsilon(1-\epsilon)[\epsilon^2 + (1-\epsilon)^2]}{3} + \epsilon^4\left(\frac{\pi}{4} - \frac{8}{9\pi}\right) + \frac{\pi\epsilon^2}{2}\left(1 - \epsilon + \frac{4\epsilon}{3\pi}\right)^2\right] \quad (33)$$

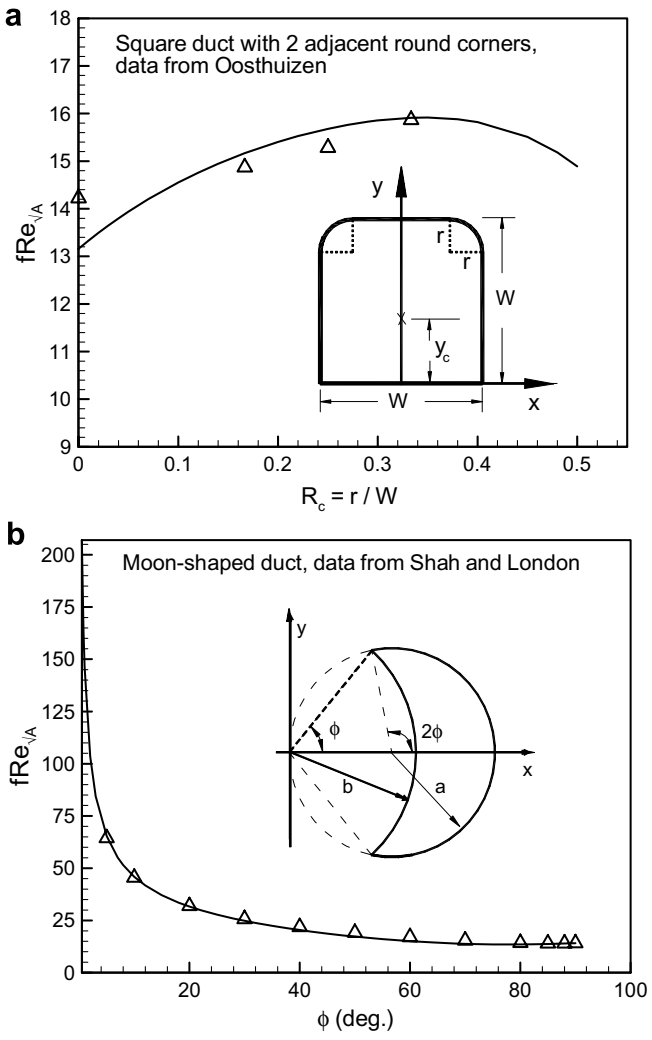

Fig. 8. Comparison of present model and numerical values for square duct with two adjacent round corners [24] and moon-shaped [18] channels.

Fig. 7b represents the comparison between the numerical results of Shah and London [18] and the present model. As seen, the present model shows excellent agreement with the numerical result with a maximum relative difference of 2.7%.

4.9. Other cross-sections

The present model is also compared with numerical results for square minichannels with two adjacent rounded corners [24] and moon-shaped ducts [18] in Fig. 8a and b, with relative differences of 2.5% and 4.8%, respectively.

5. Summary and conclusions

The pressure drop of fully developed, laminar, single-phase flow in smooth singly connected channels of arbitrary cross-sections is investigated. It is shown that the square root of the cross-sectional area $\sqrt{A}$, as the characteristic length scale, is superior to the conventional hydraulic diameter, D_h.

The analytical solution for elliptical ducts is unique since its $fRe_{\sqrt{A}}$ is only a function of the non-dimensional geometrical parameter, $I_p^*\sqrt{A}/P$, of the cross-section. Based on this observation and using the concept of Saint-Venant theorem, an novel model is developed. The proposed model is compared with experimental and numerical data for a wide variety of singly connected channels and microchannels, cross-sections such as: rectangle, triangle, hyperellipse, trapezoid, sine, square duct with two adjacent round corners, rhombic, circular sector, circular segment, annular sector, rectangle with semi-circular ends, and moon-shaped. The model successfully predicts the pressure drop for these shapes with relative differences on the order of 8%. This "bottom-up" approach clearly demonstrates a common trend in cross-sections considered and that the proposed model can be used to accurately estimate the pressure drop of laminar, fully developed flow in microchannels of arbitrary cross-sections.

Acknowledgements

The authors gratefully acknowledge the financial support of the Centre for Microelectronics Assembly and Packaging, CMAP and the Natural Sciences and Engineering Research Council of Canada, (NSERC).

References

[1] C.S. Chen, W.J. Kuo, Heat transfer characteristics of gaseous flow in long mini- and microtubes, Numer. Heat Transfer, Part A: Appl. 45 (5) (2004) 497–514.
[2] G. Maranzana, I. Perry, D. Maillet, Modeling of conjugate heat transfer between parallel plates separated by a hydrodynamically developed laminar flow by the quadrupole method, Numer. Heat Transfer, Part A: Appl. 46 (2) (2004) 147–465.
[3] H. Sun, M. Faghri, Effects of rarefaction and compressibility of gaseous flow in microchannel using DSMC, Numer. Heat Transfer, Part A: Appl. 38 (2) (2000) 153–168.
[4] H. Sun, M. Faghri, Effects of surface roughness on nitrogen flow in a microchannel using the direct simulation Monte Carlo method, Numer. Heat Transfer, Part A: Appl. 43 (1) (2003) 1–8.
[5] A. Beskok, Validation of a new velocity-slip model for separated gas microflow, Numer. Heat Transfer, Part B: Fundam. 40 (6) (2001) 451–471.
[6] C. Yang, J. Wu, H. Chien, S. Lu, Friction characteristics of water, R-134a, and air in small tubes, Microscale Thermophys. Eng. 7 (2003) 335–348.
[7] G.L. Morini, Laminar-to-turbulent flow transition in microchannels, Microscale Thermophys. Eng. 8 (2004) 15–30.
[8] R. Baviere, F. Ayela, S. Le Person, M. Favre-Marinet, Experimental characterization of water flow through smooth rectangular microchannels, Phys. Fluids 17 (2005) 098105-1-4.
[9] K.V. Sharp, R.J. Adrian, Transition from laminar to turbulent flow in liquid filled microtubes, Exp. Fluids 36 (5) (2004) 741–747.
[10] J. Judy, D. Maynes, B.W. Webb, Characterization of frictional pressure drop for liquid flows through microchannels, Int. J. Heat Mass Transfer 45 (2002) 3477–3489.
[11] P.S. Lee, S. Garimella, D. Liu, Investigation of heat transfer in rectangular microchannels, Int. J. Heat Mass Transfer 48 (9) (2005) 1688–1704.

[12] D. Pfund, D. Rector, A. Shekarriz, A. Popescu, J. Welty, Pressure drop measurements in a microchannel, AICHE J. 46 (8) (2000) 1496–1507.
[13] D. Liu, S. Garimella, Investigation of liquid flow in microchannels, J. Thermophys. Heat Transfer, AIAA 18 (1) (2004) 65–72.
[14] H.Y. Wu, P. Cheng, Friction factors in smooth trapezoidal silicon microchannels with different aspect ratios, Int. J. Heat Mass Transfer 46 (2003) 2519–2525.
[15] M. Bahrami, M.M. Yovanovich, J.R. Culham, Pressure drop of fully developed, laminar flow in rough microtubes, ASME J. Fluids Eng. 128 (2006) 632–637.
[16] Y.S. Muzychka, M.M. Yovanovich, Solution of Poisson equation within singly and doubly connected prismatic domains, Paper No. AIAA97-3880, In: Proceedings of National Heat Transfer Conference, Baltimore, MD, August 10–12, 1997.
[17] Y.S. Muzychka, M.M. Yovanovich, Laminar flow friction and heat transfer in non-circular ducts and channels part 1: Hydrodynamic problem, in: Proceedings of Compact Heat Exchangers, A Festschrift on the 60th Birthday of Ramesh K. Shah, Grenoble, France, 2002, pp. 123–130.
[18] R.K. Shah, A.L. London, Laminar Flow Forced Convection in Ducts, Academic Press, New York, 1978 (Chapter 10).
[19] Frank M. White, Viscous Fluid Flow, McGraw-Hill Inc., New York, 1974 (Chapter 3).
[20] M.M. Yovanovich, Advanced Heat Conduction, in preparation (Chapter 12).
[21] S.P. Timoshenko, J.N. Goodier, Theory of Elasticity, McGraw-Hill Inc., New York, 1970 (Chapter 10).
[22] R.C. Hibbeler, Engineering Mechanics Statics and Dynamics, Pearson, Prentice Hall, Upper Saddle River, U.S.A., 2004.
[23] P. Gao, S. Le Person, M. Favre-Marinet, Scale effects on hydrodynamics and heat transfer in two-dimensional mini and microchannels, Int. J. Therm. Sci. 41 (2002) 1017–1027.
[24] P.H. Oosthuizen, Flow and heat transfer in a square minichannel with rounded corners, in: ASME Third International Conference on Microchannels, July 13–15, University of Toronto, Canada, 2005.
[25] M.M. Yovanovich, S.S. Burde, J.C. Thompson, Thermal constriction resistance of arbitrary planar contacts with constant flux, AIAA, Paper No. 76-440, 56 (1976) 126–139.